Local Sn Dipolar-Character Displacements behind the Low Thermal Conductivity in SnSe Thermoelectric

E. S. Bozin, H. Xie, A. M. M. Abeykoon, S. M. Everett, M. G. Tucker, M. G. Kanatzidis, and S. J. L. Billinge

Phys. Rev. Lett. **131**, 036101 — Published 17 July 2023

DOI: 10.1103/PhysRevLett.131.036101

Local Sn dipolar-character displacements behind the low thermal conductivity in SnSe thermoelectric

E. S. Bozin,[1,*] H. Xie,[2] A. M. M. Abeykoon,[3] S. M. Everett,[4] M. G. Tucker,[4] M. G. Kanatzidis,[2] and S. J. L. Billinge[5]

[1] *Condensed Matter Physics and Materials Science Division, Brookhaven National Laboratory, Upton, NY 11973, USA*
[2] *Department of Chemistry, Northwestern University, Evanston, Illinois 60208, USA*
[3] *Photon Sciences Division, Brookhaven National Laboratory, Upton, New York 11973, USA*
[4] *Neutron Scattering Division, Oak Ridge National Laboratory, Oak Ridge, Tennessee 37831, USA*
[5] *Department of Applied Physics and Applied Mathematics, Columbia University, New York, NY 10027, USA*

(Dated: June 16, 2023)

The local atomic structure of SnSe was characterized across its orthorhmbic-to-orthorhombic structural phase transition using x-ray pair distribution function analysis. Substantial Sn displacements with a dipolar character persist in the high symmetry high temperature phase, albeit with a symmetry different from that of the ordered displacements below the transition. The analysis implies that the transition is neither order-disorder nor displacive, but rather a complex crossover. Robust ferro-coupled SnSe intra-layer distortions suggest a ferroelectric-like instability as the driving force. These local symmetry-lowering Sn displacements are likely integral to the ultra-low lattice thermal conductivity mechanism in SnSe.

Suppression of heat transport is critical [1] to high performance thermoelectricity [2], requiring the ability to effectively scatter heat-bearing phonons [3–9]. This can be accomplished either via crystal engineering [10–14], or by utilization of materials with intrinsically low lattice thermal conductivity [15, 16]. In the latter case, particularly intriguing are systems exhibiting nanoscale symmetry-broken states that are intrinsic and driven by electronic instabilities. For example, in thermoelectric PbTe such a state emerges on warming and involves fluctuating Pb dipolar-like displacements [17] and associated giant anharmonic phonon scattering [18, 19]. The actual situation in that material is complex and has required detailed followup studies [20–25] with complementary techniques and theory, offering explanations in terms of the stereochemistal activity of $6s^2$ electron lone pairs [26] and related resonant/metavalent bonding ideas[27]. A somewhat similar emergent state was found in $AgGaTe_2$, where local displacements of Ag were driven by a weak sd^3 orbital hybridization, resulting in strong acoustic-optical phonon scattering and an ultralow lattice thermal conductivity [28], highlighting the diversity of electronic instabilities that can lead to hidden nanostructural responses.

Here we address the binary semiconductor SnSe, Fig. 1(a) [29], a novel high efficiency high temperature thermoelectric exhibiting ultralow thermal conductivity and high thermoelectric figure of merit ZT [30, 31]. Due to its remarkable optoelectronic properties, SnSe has also been extensively explored for photovoltaic applications [32–36], whereas its monolayer variants feature robust and tunable ferroelectricity [37–40]. The material has a simple structure featuring two-dimensional (2D) bilayers. At low temperature it forms an orthorhombic structure in the Pnma space group. It has a structural phase transition to a higher symmetry but also orthorhombic (Cmcm) structure, Fig. 1(b), at $T_s \approx 800$ K [41–43]. As with the above examples, a complex interplay of lattice and electronic degrees of freedom are at play, in this case involving $5s^2$ Sn electron lone pairs [44], multiple band edges [45, 46], and highly anisotropic bonding [47]. A large lattice anharmonicity exhibited by the high-energy optical phonons and driven by a ferroelectric-like instability [48, 49] has been observed. Recent first-principles calculations [50] suggested that a Jahn-Teller-like instability of the band structure causes a lattice distortion in the vicinity of the structural transition whose coupling to lattice dynamics results in the observed strong anharmonicity and the ultralow thermal conductivity. We investigate this further using the atomic pair distribution function (PDF) technique [51] a probe of local structure.

We find that, in the high symmetry Cmcm phase, the local structure displays a complex evolution of Sn displacements away from the position implied by the average structure obtained from Bragg scattering, likely fluctuating in time, which persists on a nanometer length scale up to at least 1070 K. The phase transition cannot be regarded as order-disorder, since the local distortions at high T are of different symmetry and magnitude than those observed below T_s.

A polycrystalline SnSe sample was synthesized using the approach reported in Ref. 47. It behaves canonically as determined by an average structure analysis of the sample through Rietveld refinements [52] of neutron powder diffraction data collected at beamline BL-1B at the Spallation Neutron Source (SNS) over $300 \leq T \leq 975$ K range in steps of $\Delta T = 25$ K. The Bragg analysis confirmed the Pnma and Cmcm structures below and above T_s, respectively, Fig. 1(c), (d).

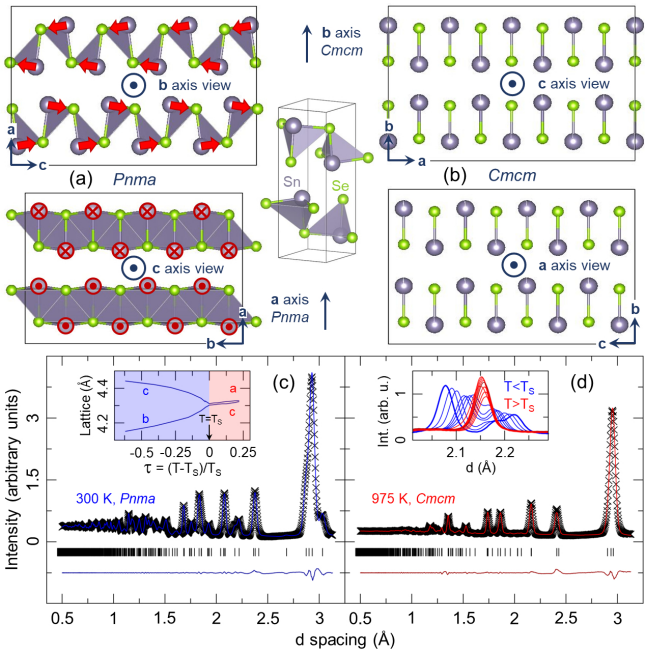

FIG. 1. Crystal structure of SnSe and temperature induced phase transition. The structure features two SnSe bilayers which are related by inversion symmetry. (a) Low temperature Pnma phase. Sn is displaced from the center of the plaquette of Se ions forming strongly bonded $SnSe_3$ pyramids. The associated atomic dipolar displacements exhibit intra-bilayer "ferro" and inter-bilayer "antiferro" ordering, as indicated by the red arrows. (b) High temperature Cmcm phase. Sn is centered in the plaquette on average, resulting in a Sn-Se dumbbell motif when viewed down the c-axis, the apical Sn-Se being the shortest bond in the structure. To enable comparison in (a) and (b), an arbitrary stack of unit cells, depicted in the middle for Pnma, along the bilayer directions is shown. Rietveld fits of neutron powder diffraction data confirm the average sample structure across the transition: Pnma at 300 K (c) and Cmcm at 975 K (d). Evolution of the in-plane lattice parameters and the Cmcm (200)/(002) reflection across the transition ($T_s \approx 840$ K) are shown in the insets to (c) and (d).

The Pnma crystal structure contains two SnSe bilayers in the unit cell, featuring intra-bilayer ferro-ordered Sn displacements and exhibiting inter-bilayer antiferro-coupling, as shown in Fig. 1(a). The primary component of the distortion is a displacement of Sn from the center of the square formed by its almost coplanar Se ions (Fig. 2(i)). In the Cmcm average structure by Bragg scattering, Fig. 1(b), the Sn is centered in the plaquette with four equal bond-lengths to its coplanar Se ions (Fig. 2(j)).

In the Rietveld refinements of the Cmcm phase, we found substantially enlarged and nearly isotropic planar components of Sn's atomic displacement parameters (ADPs). At 975 K, $U_{11} = 0.075(2)$ Å^2 and $U_{33} = 0.078(3)$ Å^2, whereas $U_{22} = 0.040(3)$ Å^2 in the direction perpendicular to the bilayers. This is consistent with a high resolution powder diffraction report [43] and indicative of intra-bilayer structural disorder at high T, suggestive of an order-disorder character of the structural transition that should be evident in the local structure.

For the local structural studies we carried out x-ray total scattering experiments in the range $300 \leq T \leq 1070$ K in steps of $\Delta T = 5$ K at the 28-ID-1 (PDF) beamline at the National Synchrotron Light Source II (NSLS-II) using a 74.5 keV energy beam ($\lambda = 0.1665$ Å, $Q_{max} = 25$ Å^{-1}) in rapid acquisition mode [53] using a 2D PerkinElmer area detector. For further details please see the SI. Finely pulverized SnSe powder was loaded in an evacuated and flame-sealed quartz capillary with inner diameter of 1 mm. Sample temperature control on warming was achieved using a FMB Oxford Hot Air Blower model GSB1300. The PDFs, $G(r)$, were obtained using standard protocols [54, 55] with the help of the xPDFsuite program [56] and modelled over different r-ranges using the PDFgui program [57].

To see how the PDFs would behave based on the average crystal structure through the phase transition, in Fig. 2(b) we show PDFs computed from the Rietveld models at selected temperatures below and above T_s [43]. The actual measured PDFs are shown in Fig. 2(c). The observed changes in the PDFs with temperature are similar in the two cases. However, the changes are different in detail in the region of the PDF, $2.8 \leq r \leq 3.3$ Å, that describes the Sn-Se planar bonds. In the average structure from Bragg scattering, this peak shifts in position to higher-r as the sample goes through the phase transition. This is because the average Sn off-centering reduces in amplitude with increasing temperature, disappearing completely for $T > T_s$. The solid red arrow at ~ 3.1 Å in Fig. 2(b) highlights this. Simultaneously, the peaks at $r \sim 2.8$ Å and at ~ 3.4 Å reduce strongly in intensity. This is also reflected in the loss of the sinusoidal diffuse scattering in F(Q) on warming (Figs. 3 and S5, and discussion around this figure in the SI). This response in the PDF computed from the average structure from Bragg scattering comes from Sn-Se planar bonds going from 2-short, 2-long in the Pnma structure to 4-medium (~ 3.1 Å) bonds in Cmcm. This is shown schematically in Figs. 2(i) and 2(j).

On the other hand, this is not seen in the measured total scattering PDFs. The peaks at $r \sim 2.8$ and 3.3 Å broaden with increasing temperature, but they do not shift and no additional intensity grows up at the average $r \sim 3.1$ Å position. The local environment of the Sn does not change significantly with temperature from the Pnma phase all the way up to 1070 K (dashed dark red trace in Figs. 2(c)) and S4. We next turn to modeling to quantify and characterize this behavior.

The effect observed in the qualitative analysis is clear also in the modeling. At low temperature, the Pnma model fits well over the entire range of the PDF, as evidenced by the small agreement factor (7.1 %) and the lack

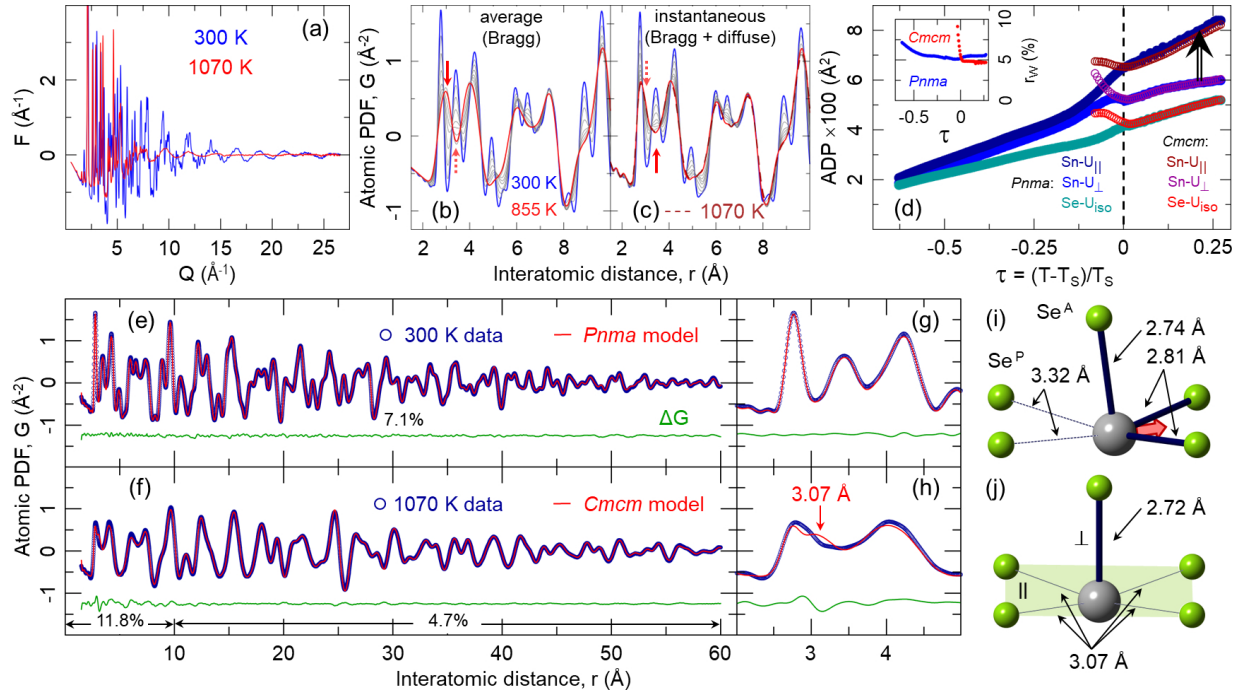

FIG. 2. Assessment of the structure of SnSe over different length scales. (a) Measured reduced x-ray total scattering function, $F(Q)$, at 300 K (blue) and 1070 K (red). (b) and (c). Representative PDFs from different temperatures are shown (b) calculated from the average structure by Bragg scattering fits [43] (see SI for more information), and (c) from total scattering measurements. The PDFs from the extremal temperatures are plotted in red (hot) and blue (cool) colors. Intermediate temperatures are shown in gray. Solid/dotted red arrows indicate presence/absence of features discussed in the text. (d) Temperature evolution of atomic displacement parameters (ADPs) obtained from Pnma and Cmcm PDF models fit over the r-range $10 \leq r \leq 60$ Å. The abscissa is the reduced temperature, $\tau = (T - T_s)/T_s$, where T_s is the phase transition temperature. Different colored curves are from anisotropic Sn ADPs with components parallel and perpendicular to the layers, and isotropic Se ADPs, as indicated. A sizeable enhancement of the in-plane ADP component is seen at $T > T_s$, marked by a black arrow, indicative of planar disordering of the Sn in the high temperature phase. The inset shows the fit residual, $r_w(T)$, for the two models. Fits of average structure models over the entire r-range for 300 K and 1070 K are shown in (e) in (f), respectively. Difference traces between the calculated and measured PDF, ΔG, in green are offset for clarity. In panels (g) and (h) the same fits are shown expanded on the low-r region. An observable discrepancy is seen between the Cmcm model and 1070 K data on a sub-nanometer length scale, resulting in an increase of r_w. The Sn environments expected from the average structure by Bragg scattering are depicted in (i) and (j). In the Pnma structure the Sn is displaced sideways from being directly below Se, whereas in the Cmcm average structure the Sn is directly below it. Labels A and P refer to apical and in-plane Se, respectively. The arrow in (h) marks a feature expected in the Cmcm symmetry model, associated with the Sn being centered in the Se plaquette, which is clearly absent in the data.

of structure in the residual plotted in green and labeled ΔG in Fig. 2(e). On the other hand, at high temperature in the Cmcm phase, fitting the Cmcm model to the measured PDF results in a very good fit in the high-r region (> 10 Å), but the fit becomes poor in the region below 10 Å. The average Cmcm structure is not describing the local structure well in the Cmcm phase. The nature of the failure is highlighted in Fig. 2(h) and indeed, there is a lack of intensity at the average Sn-Se square-planar distance of 3.07 Å. In the local structure the total scattering results indicate that the Sn makes large dipolar deviations away from the center of the square of Se ions even in the Cmcm phase.

The temperature dependence of the offsets can be seen reflected in fits to the PDF of Sn ADPs of Pnma and Cmcm models over the $10 \leq r \leq 60$ Å range, shown in Fig. 2(b). X-ray PDF derived ADPs from mixed systems may not be accurate on an absolute scale due to the Morningstar-Warren approximation [51] but their temperature dependence can be a reliable indicator of nonharmonic effects [17, 58]. Nonetheless, the result is supported by Rietveld refinements of the ADPs shown in Fig. S3. The ADP of Se does not behave anomalously and is almost linear all the way into the Cmcm phase. The component of the Sn ADP perpendicular to the layers is also well-behaved. However, the in-plane component of the Sn ADP is higher than the other two and increases as the sample passes into the Cmcm phase, again supporting the idea that the Sn resides predominantly in positions away from the center of the Se plaquette. This is consistent with a previously reported gradual deviation of ADPs from these predicted by the Debye model

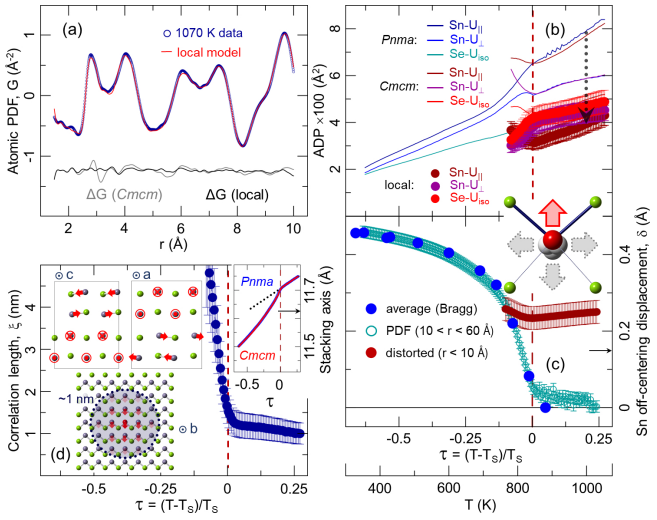

FIG. 3. Local symmetry breaking Sn displacements in SnSe at $T > T_s$. (a) The fit to 1070 K data of the local distorted model (shown in the inset to (b) and (c)) featuring split Sn sites. The corresponding difference trace, ΔG (black), is offset for clarity. The gray difference trace is that of the Cmcm model from Fig. 2, which is shown as a reference. (b) The distorted model, labelled here as "local", results in ADP magnitudes substantially reduced as compared to these observed by undistorted models. The ADPs obtained from Pnma and Cmcm shown in Fig. 2(d), are reproduced as solid lines. (c) The magnitude of the Sn displacements away from the center of the plaquette vs. reduced temperature, and absolute temperature, as seen by high resolution powder diffraction [43], and $10 \leq r \leq 60$ Å range PDF Pnma model fits. The Se_4 plaquette is nearly a square in Cmcm and, to preserve the average symmetry, the local model allows for displacements in 4 directions indicated by block-arrows in the inset. (d) The estimated correlation length of local distortions, as described in the text. Insets to the left: the displacement coupling, shown in a $2 \times 1 \times 2$ Cmcm supercell, of the best model where the couplings are explicitly tested. Inset to the right: temperature dependent lattice parameter along the bilayer stacking direction (b axis of Cmcm model in red, a axis of Pnma model in blue). Note the change in slope at temperature T_s.

as the transition is approached on warming [43].

The simplest explanation for the observed behavior is that the phase transition has an order-disorder character and the Pnma distortions survive to high-T but become disordered among the different variants. More detailed modeling can establish if this is indeed the case. Different distorted local models were initially fit to the 1070 K data over the narrow r-range ($1.5 \leq r \leq 10$ Å) where the misfits in the Cmcm model are seen.

The model featuring Pnma symmetry with ferro-coupled displacements along the b-axis and within the bilayer, Fig. 1(a), resulted in an improved fit residual compared to Cmcm (7.5 % vs. 11.8%). However, this model did not fully account for the observed misfit seen in Figs. 2(f) and (h) and returned a dramatically enlarged intra-layer ADP in the direction perpendicular to the Sn displacement. This is inconsistent with isotropic intra-layer ADPs observed in broad range fits described above, implying that there is a distortion component in the Cmcm phase also along the c-axis, which is not accounted for by the Pnma symmetry. Constraining the intra-layer ADPs to be isotropic resulted in similar issues. This is not a purely order-disorder transition.

A split site model, depicted in the inset to Fig. 3(b), was introduced next, in which isotropy of intra-layer ADPs was maintained. In this, each of the crystallographic Sn and Se sites within the Cmcm symmetry was split into four equally populated sites (25 % occupancy each). Each site of the same type (Sn or Se) in the model was allocated the same displacement parameter away from the centered Cmcm configuration and along both a and c crystallographic directions. This model resulted in a fit with appreciably improved residual (5.8 %), Fig. 3(a), and significantly reduced ADPs, Fig. 3(b). Notably, the temperature dependence of the observed values of ADPs at high temperature agree well with the Debye model prediction [43]. The model yielded Sn displacements, δ, of ~ 0.25 Å, and an order of magnitude smaller Se displacements (~ 0.02 Å). This suggests dynamic motions of displaced Sn ions in something reminiscent of a Mexican hat potential occurring in the Cmcm phase, similar to the high temperature phase of hexagonal manganites [59]. This model was then applied to all high temperature data. Nearly temperature-independent Sn displacements ensued, as shown in Fig. 3(c). On the other hand, the fit of the split site model significantly deteriorated below T_s (Fig. S7) implying that the local distortion symmetry starts changing at the transition.

The temperature dependence of the spatial correlations of the local distortions, ξ, was estimated from the r-dependent (cumulative) integrals of the absolute value of the difference between the data and the Cmcm model, $|\Delta G(r)|$, over the full range of data up to 60 Å. The process of estimating ξ is illustrated in Fig. S6. The characteristic length scale of short-range correlations is defined as the value of r at which the integral departs from a linear trend associated with statistical noise in the PDF data [60]. In Fig. 3(d), $\xi(T)$ increases slowly on decreasing temperature for $T > T_s$, but exhibits a rapid increase at $T < T_s$. This behavior is highly unusual. If the local distortions were related to critical fluctuations of the Pnma phase, it would be expected that their correlation length diverges at T_s as this is approached from above. This is clearly not the case, as $\xi(T)$ exhibits a rapid upturn at and *below* T_s. The distortions associated with disorder at $T > T_s$ are therefore likely not directly related to the instability driving the Pnma ordering, further corroborating the conclusion that the transition is not of conventional order-disorder type.

Models incorporating different combinations of displacement patterns involving two bilayers have also been tested against the high temperature data. In these mod-

els, displacements were allowed to be ferro- or antiferro-coupled within individual layers of the bilayers, with inter-bilayer ferro- or antiferro-coupling. These short range models resulted in fits of similar quality (See SI for details). The model involving a pattern with ferro-coupled distortions within individual sub-layers within the bilayer, and antiferro-coupling between the sub-layers in the bilayer, sketched in the inset to Fig. 3(d), resulted in the lowest r_w, with fit residual and ADPs comparable to those observed by the split site model (5.5 %). The data suggest that on a nanometer length scale at high temperature, the 2D ferro-coupling within the bilayers survives but the 3D ordering is lost, in contrast to the robust 3D-like ferro intra-bilayer coupling observed in the Pnma phase. It is tempting to speculate that the origin of the phase transition is a 2D-3D crossover, where somewhat robust fluctuating 2D locally-ferro-coupled intra-bilayer dipoles persist at all temperatures but only order into a static structure when a much weaker perpendicular coupling is able to drive the ordering. This dimensionality crossover might be supported by the observation of a sharp change in the temperature dependence of the lattice parameter in the stacking direction at the transition (upper right inset to Fig. 3(d) and Fig. S2 in the SI). The behavior is seen whether the data are modeled with the Pnma or the Cmcm models and it shows a rapid expansion along the stacking direction in the ordered Pnma phase but a much slower expansion above the transition. Understanding this will require more studies such as 3D-ΔPDF measurements.

Another notable observation is that the anomalous upturn in ADPs on warming starts at $\sim$ 600 K [43], well below the phase transition (-0.25 in reduced temperature units), suggesting that the dynamic disorder is setting in even while there remains a net long-range ordered off centered Sn displacement with the Pnma character.

In summary, we have shown that, in the vicinity of and above the phase transition where the thermoelectricity is very good, SnSe is nanostructured with electronically driven intrinsic fluctuating Sn dipolar character displacements. These are short-range correlated with ferro-ordering preferred within a single layer within the bilayers but with an apparent loss of coherence of the dipole ordering along the stacking direction even within the bilayer.

Work at Brookhaven National Laboratory (BNL), and access to the 28ID-1 beamline at NSLS-II, was supported by U.S. Department of Energy, Office of Science, Office of Basic Energy Sciences (DOE-BES) under contract No. DE-SC0012704. MGK acknowledges partial support from DOE-BES under grant DE-SC0014520. Neutron powder diffraction data were collected at BL-1B beamline of the SNS, a DOE-BES User Facility operated by the Oak Ridge National Laboratory.

* bozin@bnl.gov

[1] G. Nolas, J. Poon, and M. Kanatzidis, MRS Bull. **31**, 199 (2006), URL https://www.cambridge.org/core/journals/mrs-bulletin/article/abs/recent-developments-in-bulk-thermoelectric-materials/1B7FC5CB023D6847E8368A49F63259BE.

[2] G. D. Mahan and J. O. Sofo, Proc. Natl. Acad. Sci. **93**, 7436 (1996), URL https://www.pnas.org/doi/abs/10.1073/pnas.93.15.7436.

[3] B. C. Sales, MRS Bull. **23**, 15 (1998), URL https://www.cambridge.org/core/journals/mrs-bulletin/article/abs/electron-crystals-and-phonon-glasses-a-new-path-to-improved-thermoelectric-materials/E0943BD4A1E605D54353CF7360FAA08C.

[4] G. S. Nolas, D. T. Morelli, and T. M. Tritt, Annu. Rev. Mater. Sci. **29**, 89–116 (1999), URL https://www.annualreviews.org/doi/abs/10.1146/annurev.matsci.29.1.89.

[5] G. J. Snyder, M. Christensen, E. Nishibori, T. Caillat, and B. B. Iversen, Nat. Mater. **3**, 458–463 (2004), URL https://www.nature.com/articles/nmat1154.

[6] D. T. Morelli, V. Jovovic, and J. P. Heremans, Phys. Rev. Lett. **101**, 035901 (2008), URL https://link.aps.org/doi/10.1103/PhysRevLett.101.035901.

[7] K. Miyata, T. L. Atallah, and X.-Y. Zhu, Sci. Adv. **3**, e1701469 (2017), URL https://www.science.org/doi/abs/10.1126/sciadv.1701469.

[8] D. J. Voneshen, H. C. Walker, K. Refson, and J. P. Goff, Phys. Rev. Lett. **118**, 145901 (2017), URL https://link.aps.org/doi/10.1103/PhysRevLett.118.145901.

[9] K. Zhao, P. Qiu, X. Shi, and L. Chen, Adv. Funct. Mater. **30**, 1903867 (2020), URL https://onlinelibrary.wiley.com/doi/full/10.1002/adfm.201903867.

[10] K. F. Hsu, S. Loo, F. Guo, W. Chen, J. S. Dyck, C. Uher, T. Hogan, E. K. Polychroniadis, and M. G. Kanatzidis, Science **303**, 818 (2004), URL https://www.science.org/doi/abs/10.1126/science.1092963.

[11] R. Liu, H. Chen, K. Zhao, Y. Qin, B. Jiang, T. Zhang, G. Sha, X. Shi, C. Uher, W. Zhang, et al., Adv. Mater. **29**, 1702712 (2017), URL https://onlinelibrary.wiley.com/doi/abs/10.1002/adma.201702712.

[12] D. J. Voneshen, K. Refson, E. Borissenko, M. Krisch, A. Bosak, A. Piovano, E. Cemal, M. Enderle, M. J. Gutmann, M. Hoesch, et al., Nat. Mater. **12**, 1028–1032 (2013), URL https://www.nature.com/articles/nmat3739.

[13] Y. Zheng, Q. Zhang, X. Su, H. Xie, S. Shu, T. Chen, G. Tan, Y. Yan, X. Tang, C. Uher, et al., Adv. Energy Mater. **5**, 1401391 (2015), URL https://onlinelibrary.wiley.com/doi/abs/10.1002/aenm.201401391.

[14] Z. Chen, B. Ge, W. Li, S. Lin, J. Shen, Y. Chang, R. Hanus, G. J. Snyder, and Y. Pei, Nat. Commun. **8**, 13828 (2019), URL https://www.nature.com/articles/ncomms13828.

[15] H. Liu, X. Shi, F. Xu, L. Zhang, W. Zhang, L. Chen, Q. Li, C. Uher, T. Day, and G. J. Snyder, Nat. Mater. **11**, 422–425 (2012), URL https://www.nature.com/articles/nmat3273.

[16] T. Takabatake, K. Suekuni, T. Nakayama, and E. Kaneshita, Rev. Mod. Phys. **86**, 669 (2014), URL https://link.aps.org/doi/10.1103/RevModPhys.86.669.

[17] E. S. Bozin, C. D. Malliakas, P. Souvatzis, T. Proffen, N. A. Spaldin, M. G. Kanatzidis, and S. J. L. Billinge, Science **330**, 1660 (2010), URL https://www.science.org/doi/10.1126/science.1192759.

[18] O. Delaire, J. Ma, K. Marty, A. F. May, M. A. McGuire, M. Du, D. J. Singh, A. Podlesnyak, G. Ehlers, M. D. Lumsden, et al., Nat. Mater. **10**, 614–619 (2011), URL https://www.nature.com/articles/nmat3035.

[19] K. M. O. Jensen, E. S. Bozin, C. D. Malliakas, M. B. Stone, M. D. Lumsden, M. G. Kanatzidis, S. M. Shapiro, and S. J. L. Billinge, Phys. Rev. B **86**, 085313 (2012), URL https://link.aps.org/doi/10.1103/PhysRevB.86.085313.

[20] C. M. Zeuthen, e. S. Thorup, N. Roth, and B. B. Iversen, J. Am. Chem. Soc. **141**, 8146 (2019), URL https://pubs.acs.org/doi/full/10.1021/jacs.9b00043.

[21] K. A. U. Holm, N. Roth, C. M. Zeuthen, K. Tolborg, A. A. Feidenhans'l, and B. B. Iversen, Phys. Rev. B **102**, 024112 (2020), URL https://link.aps.org/doi/10.1103/PhysRevB.102.024112.

[22] K. A. U. Holm, N. Roth, C. M. Zeuthen, and B. B. Iversen, Phys. Rev. B **103**, 224302 (2021), URL https://link.aps.org/doi/10.1103/PhysRevB.103.224302.

[23] M. D. Nielsen, V. Ozolins, and J. P. Heremans, Energy Environ. Sci. **6**, 570 (2013), URL https://pubs.rsc.org/en/content/articlelanding/2013/ee/c2ee23391f.

[24] B. Sangiorgio, E. S. Bozin, C. D. Malliakas, M. Fechner, A. Simonov, M. G. Kanatzidis, S. J. L. Billinge, N. A. Spaldin, and T. Weber, Phys. Rev. Mater. **2**, 085402 (2018), URL https://link.aps.org/doi/10.1103/PhysRevMaterials.2.085402.

[25] Z. Chen, Z. Jian, W. Li, Y. Chang, B. Ge, R. Hanus, J. Yang, Y. Chen, M. Huang, G. J. Snyder, et al., Adv. Mater. **29**, 1606768 (2017), URL https://onlinelibrary.wiley.com/doi/10.1002/adma.201606768.

[26] A. Walsh, D. J. Payne, R. G. Egdell, and G. W. Watson, Chem. Soc. Rev. **40**, 4455 (2011), URL https://pubs.rsc.org/en/content/articlelanding/2011/CS/c1cs15098g.

[27] B. J. Kooi and M. Wuttig, Adv. Mater. **32**, 1908302 (2020), URL https://onlinelibrary.wiley.com/doi/10.1002/adma.201908302.

[28] H. Xie, E. S. Bozin, Z. Li, M. Abeykoon, S. Banerjee, J. P. Male, G. J. Snyder, C. Wolverton, S. J. L. Billinge, and M. G. Kanatzidis, Adv. Mater. **34**, 2202255 (2022), URL https://onlinelibrary.wiley.com/doi/10.1002/adma.202202255.

[29] A. Okazaki and I. Ueda, J. Phys. Soc. JPN **11**, 470 (1956), URL https://doi.org/10.1143/JPSJ.11.470.

[30] L. Zhao, S. Lo, Y. Zhang, H. Sun, G. Tan, C. Uher, C. Wolverton, V. P. Dravid, and M. G. Kanatzidis, Nature **508**, 373 (2014), URL https://www.nature.com/articles/nature13184.

[31] L. Zhao, G. Tan, S. Hao, J. He, Y. Pei, H. Chi, H. Wang, S. Gong, H. Xu, V. P. Dravid, et al., Science **351**, 141 (2016), URL https://www.science.org/doi/10.1126/science.aad3749.

[32] F. K. Butt, M. Mirza, C. Cao, F. Idrees, M. Tahir, M. Safdar, Z. Ali, M. Tanveer, and I. Aslam, CrystEngComm **16**, 3470 (2014), URL https://pubs.rsc.org/en/content/articlelanding/2014/CE/c4ce00267a.

[33] S. Zhao, H. Wang, Y. Zhou, L. Liao, Y. Jiang, X. Yang, G. Chen, M. Lin, Y. Wang, H. Peng, et al., Nano Res. **8**, 288–295 (2015), URL https://link.springer.com/article/10.1007/s12274-014-0676-8.

[34] F. Liu, J. Zhu, Y. Xu, L. Zhou, Y. Li, L. Hu, J. Yao, and S. Dai, Chem. Commun. **51**, 8108 (2015), URL https://pubs.rsc.org/en/content/articlelanding/2015/CC/C5CC00772K.

[35] V. R. Minnam Reddy, S. Gedi, B. Pejjai, and C. Park, J. Mater. Sci.: Mater. Electron. **27**, 5491 (2016), URL https://link.springer.com/article/10.1007/s10854-016-4563-9.

[36] W. Shi, M. Gao, J. Wei, J. Gao, C. Fan, E. Ashalley, H. Li, and Z. Wang, Adv. Sci. **5**, 1700602 (2018), URL https://onlinelibrary.wiley.com/doi/full/10.1002/advs.201700602.

[37] K. Chang, F. Küster, B. J. Miller, J. Ji, J. Zhang, P. Sessi, S. Barraza-Lopez, and S. S. P. Parkin, Nano Lett. **20**, 6590–6597 (2020), URL https://pubs.acs.org/doi/10.1021/acs.nanolett.0c02357.

[38] N. Higashitarumizu, H. Kawamoto, C. Lee, B. Lin, F. Chu, I. Yonemori, T. Nishimura, K. Wakabayashi, W. Chang, and K. Nagashio, Nat. Commun. **11**, 2428 (2020), URL https://www.nature.com/articles/s41467-020-16291-9.

[39] N. N. Orlova, A. V. Timonina, N. N. Kolesnikov, and E. V. Deviatov, Europhys. Lett. **135**, 37002 (2021), URL https://iopscience.iop.org/article/10.1209/0295-5075/ac2247.

[40] L. Zhu, Y. Lu, and L. Wang, J. Appl. Phys. **127**, 014101 (2020), URL https://aip.scitation.org/doi/full/10.1063/1.5123296.

[41] H. Wiedemeier and F. J. Csillag, Z. Kristallogr. **149**, 17 (1979), URL https://www.degruyter.com/document/doi/10.1524/zkri.1979.149.1-2.17/html.

[42] T. Chattopadhyay, J. Pannetier, and H. G. Von Schnering, J. Phys. Chem. Solids **47**, 879 (1986), URL https://www.sciencedirect.com/science/article/pii/0022369786900594.

[43] M. Sist, J. Zhang, and B. B. Iversen, Acta. Crystallogr. B. Struct. Sci. Cryst. Eng. Mater. **72**, 310 (2016), URL https://scripts.iucr.org/cgi-bin/paper?S2052520616003334.

[44] L. Zhao, C. Chang, G. Tan, and M. G. Kanatzidis, Energy Environ. Sci. **9**, 3044 (2016), URL https://pubs.rsc.org/en/content/articlelanding/2016/ee/c6ee01755j.

[45] D. Bansal, J. Hong, C. W. Li, A. F. May, W. Porter, M. Y. Hu, D. L. Abernathy, and O. Delaire, Phys. Rev. B **94**, 054307 (2016), URL https://link.aps.org/doi/10.1103/PhysRevB.94.054307.

[46] S. Siddique, Y. Gong, G. Abbas, M. M. Yaqoob, S. Li, S. Zulkifal, Q. Zhang, Y. Hou, G. Chen, and G. Tang, ACS Appl.

Mater. Interfaces **14**, 4091–4099 (2022), URL https://pubs.acs.org/doi/10.1021/acsami.1c20549.
[47] C. Zhou, Y. K. Lee, Y. Yu, S. Byun, Z. Luo, H. Lee, B. Ge, Y. Lee, X. Chen, O. Lee, J. Y. Cojocaru-Mirédin, et al., Nat. Mater. **20**, 1378–1384 (2021), URL https://www.nature.com/articles/s41563-021-01064-6.
[48] C. W. Li, J. Hong, A. F. May, D. Bansal, S. Chi, T. Hong, G. Ehlers, and O. Delaire, Nat. Phys. **11**, 1063–1069 (2015), URL https://www.nature.com/articles/nphys3492.
[49] F. Serrano-Sánchez, M. Gharsallah, N. Nemes, F. Mompean, J. L. Martínez, and J. A. Alonso, Appl. Phys. Lett. **106**, 083902 (2015), URL https://aip.scitation.org/doi/10.1063/1.4913260.
[50] J. Hong, Delaire, and O. Delaire, Mater. Today Phys. **10**, 100093 (2019), URL https://www.sciencedirect.com/science/article/pii/S2542529318301251.
[51] T. Egami and S. J. L. Billinge, *Underneath the Bragg peaks: structural analysis of complex materials* (Elsevier, Amsterdam, 2012), 2nd ed., URL http://store.elsevier.com/product.jsp?lid=0\&iid=73\&sid=0\&isbn=9780080971414.
[52] B. H. Toby and R. B. Von Dreele, J. Appl. Cryst. **46**, 544 (2013), URL https://onlinelibrary.wiley.com/iucr/doi/10.1107/S0021889813003531.
[53] P. J. Chupas, X. Qiu, J. C. Hanson, P. L. Lee, C. P. Grey, and S. J. L. Billinge, J. Appl. Cryst. **36**, 1342 (2003), URL http://scripts.iucr.org/cgi-bin/paper?wf5000.
[54] P. Juhás, T. Davis, C. L. Farrow, and S. J. L. Billinge, J. Appl. Cryst. **46**, 560 (2013), URL http://dx.doi.org/10.1107/S0021889813005190.
[55] G. Ashiotis, A. Deschildre, Z. Nawaz, J. P. Wright, D. Karkoulis, F. E. Picca, and J. Kieffer, Journal of Applied Crystallography **48**, 510 (2015), ISSN 1600-5767.
[56] X. Yang, P. Juhas, C. L. Farrow, and S. J. L. Billinge, arXiv:1402.3163 [cond-mat] (2014), 1402.3163.
[57] C. L. Farrow, P. Juhás, J. Liu, D. Bryndin, E. S. Božin, J. Bloch, T. Proffen, and S. J. L. Billinge, J. Phys: Condens. Mat. **19**, 335219 (2007), URL http://iopscience.iop.org/0953-8984/19/33/335219/.
[58] I.-K. Jeong, R. H. Heffner, M. J. Graf, and S. J. L. Billinge, Physical Review B **67**, 104301 (2003).
[59] S. H. Skjærvø, Q. N. Meier, M. Feygenson, N. A. Spaldin, S. J. L. Billinge, E. S. Bozin, and S. M. Selbach, Physical Review X **9**, 031001 (2019).
[60] E. S. Božin, K. R. Knox, P. Juhás, Y. S. Hor, J. F. Mitchell, and S. J. L. Billinge, Sci. Rep. **4**, 4081 (2014), URL http://www.nature.com/srep/2014/140212/srep04081/full/srep04081.html.